Article

Porous Silicon-Based Aptasensors: Toward Cancer Protein Biomarker Detection

Sofia Arshavsky-Graham, Simon J. Ward, Naama Massad-Ivanir, Thomas Scheper, Sharon M. Weiss, and Ester Segal*

Read Online

ACCESS | Metrics & More | Article Recommendations | Supporting Information

ABSTRACT: The anterior gradient homologue-2 (AGR2) protein is an attractive biomarker for various types of cancer. In pancreatic cancer, it is secreted to the pancreatic juice by premalignant lesions, which would be an ideal stage for diagnosis. Thus, designing assays for the sensitive detection of AGR2 would be highly valuable for the potential early diagnosis of pancreatic and other types of cancer. Herein, we present a biosensor for label-free AGR2 detection and investigate approaches for enhancing the aptasensor sensitivity by accelerating the target mass transfer rate and reducing the system noise. The biosensor is based on a nanostructured porous silicon thin film that is decorated with anti-AGR2 aptamers, where real-time monitoring of the reflectance changes enables the detection and quantification of AGR2, as well as the study of the diffusion and target-aptamer binding kinetics. The aptasensor is highly selective for AGR2 and can detect the protein in simulated pancreatic juice, where its concentration is outnumbered by orders of magnitude by numerous proteins. The aptasensor's analytical performance is characterized with a linear detection range of 0.05−2 mg mL^{-1}, an apparent dissociation constant of 21 ± 1 μM, and a limit of detection of 9.2 μg mL^{-1} (0.2 μM), which is attributed to mass transfer limitations. To improve the latter, we applied different strategies to increase the diffusion flux to and within the nanostructure, such as the application of isotachophoresis for the preconcentration of AGR2 on the aptasensor, mixing, or integration with microchannels. By combining these approaches with a new signal processing technique that employs Morlet wavelet filtering and phase analysis, we achieve a limit of detection of 15 nM without compromising the biosensor's selectivity and specificity.

KEYWORDS: Optical Biosensor, Porous Silicon, Aptamer, Anterior Gradient Homologue-2, Cancer Biomarker, Label-Free, Microfluidics, Isotachophoresis
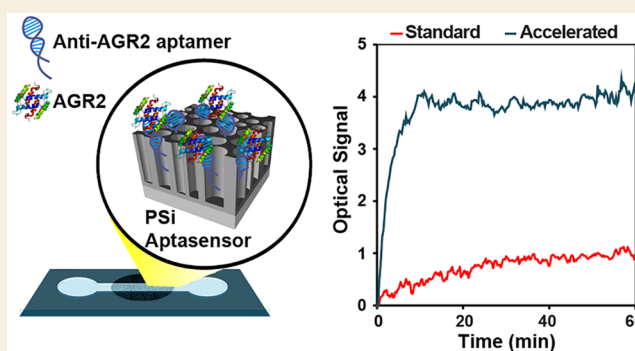
1. INTRODUCTION

The aim of biosensors for medical diagnostic applications is to detect biomarker molecules in body fluids at clinically relevant levels. In many cases, subpicomolar detection limits are required to meet the clinical criteria[1] in addition to a sufficient sensitivity (i.e., the ability to discriminate between small changes in analyte concentrations) at a low background noise. This should be accompanied by a high selectivity and a fast response time.[2−5] These three benchmarks are the main challenges to developing a successful biosensor for the clinic and should be carefully considered. For instance, overcoming the sensitivity challenge is related to maximizing the signal from a low number of analyte molecules using more sensitive transducers or amplification schemes; the latter is related to the signal or the number of target molecules.[2,5,6] A fast response time can be achieved by accelerating the mass transport of the analyte molecule to the biosensor surface, where the diffusion distance should be minimized.[2−4] Finally, selectivity, which addresses the ability to detect the presence of

the biomarker when it is outnumbered by nontarget species by several orders of magnitude, should be enhanced by minimizing the cross reactivity. This can be achieved by the proper choice of high-affinity capture probes and their density within the biosensor, tailoring the surface chemistry to minimize nonspecific adsorption, or the pretreatment of the complex biological sample to remove interfering components.[2]

The detection of protein biomarkers in body fluids for the diagnosis and prognosis of various diseases enables the development of minimally invasive and point-of-care assays. For example, screening of protein biomarkers for various types of cancer is highly valuable for cancer management and

monitoring.[1,7,8] Increasing interest has been devoted toward the protein anterior gradient homologue-2 (AGR2) over the past decade due to its diagnostic and prognostic value for pancreatic, breast, ovarian, prostate, and colorectal cancer.[9−14] Specifically in pancreatic cancer, which is one of the most lethal types of cancer, AGR2 has been suggested to play an important role in cancer initiation and development. Moreover, the level of AGR2 has been found to be elevated, at a concentration in the subnanomolar range, in the pancreatic juice of patients with high-grade pancreatic intraepithelial neoplastic lesions, which are precursors to invasive pancreatic cancer.[15−17] This would be an ideal stage for diagnosis, as it is a time point when surgical resection can potentially prevent the progression to malignancy.[17] To date, AGR2 detection has been demonstrated by traditional laboratory-based analytical methods, such as enzyme-linked immunosorbent assay (ELISA)[18] and mass spectrometry (MS),[19] which are time-consuming, laborious, and expensive. Aptamer-based optical biosensors (aptasensors) for sensitive AGR2 detection have been successfully constructed, relying on rather complex competitive reaction schemes.[20,21] Recently, a highly sensitive detection of AGR2 was demonstrated with an electrochemical immunosensor; however, selectivity was not shown in a clinically relevant medium.[22]

In this work we aim to develop a label-free biosensor for the direct detection of the protein AGR2 in body fluids. The biosensor is constructed from porous silicon (PSi) Fabry−Pérot thin films, which enable target detection via real-time monitoring of the PSi reflectance changes. Despite the significant advantages of such biosensors, their application has been rather limited due to insufficient sensitivity, usually in the micromolar range for proteins.[23−29] To the best of our knowledge, their use for detection of cancer protein biomarkers, which are usually present in the picomolar range, has not yet been demonstrated. Their inferior performance is mainly attributed to mass transfer limitations,[30−34] and several strategies have been implemented to enhance their sensitivity while still detecting the analyte in a direct and label-free manner. These include the optimization of the porous nanostructure and surface chemistry,[35−38] the design of a flow-through PSi biosensor,[32,39] microfluidic integration,[40,41] the decoration of the PSi with gold nanoparticles for an improved optical signal,[42,43] signal amplification,[44] the application of an electrokinetic focusing of the target on top of the biosensors,[31,45] and novel signal processing techniques.[46,47] Specifically, we have demonstrated the integration of PSi biosensors with the isotachophoresis (ITP) technique for on-chip analyte preconcentration and demonstrated a nanomolar detection limit for both DNA and protein targets.[31,45] Furthermore, we have recently presented a novel signal processing technique, which reduces system noise by applying Morlet wavelet convolution to filter spectra, resulting in an improved limit of detection.[47]

Herein, we investigate different avenues for enhancing the sensitivity of PSi-based biosensors and address the three key benchmarks for developing a successful biosensor.[2] The selectivity of the biosensor is achieved by the immobilization of an anti-AGR2 aptamer[48] within the PSi and is analyzed by exposing the biosensor to nontarget proteins in a buffer solution and to a simulated pancreatic juice. The sensitivity and response time of the biosensor are investigated by real-time mass transfer imaging, and several strategies for improving the protein flux to the biosensor are studied and compared.

Furthermore, a new signal processing technique is investigated to reduce the experimental noise.

2. EXPERIMENTAL SECTION

2.1. Materials

Heavily doped p-type Si wafers ($\langle 100 \rangle$-oriented, 0.90−0.95 mΩ·cm resistivity) were purchased from Sil'tronix Silicon Technologies. Aqueous HF (48%), (3-aminopropyl)triethoxysilane (APTES), diisopropylethylamine (DIEA), succinic anhydride, N-(3-(dimethylamino)propyl)-N'-ethylcarbodiimide hydrochloride (EDC), N-hydroxysuccinimide (NHS), acetonitrile (ACN), morpholinoethanesulfonic acid (MES), MES sodium salt, Tris base, and all buffer salts were purchased from Merck. Ethanol absolute was supplied by Bio-Lab Ltd. All buffer solutions were prepared with Milli-Q water (ddH$_2$O, 18.2 MΩ·cm). Polydimethylsiloxane (PDMS) was prepared from a Sylgard 184 Silicon Elastomer kit purchased from Dow Corning. The anti-AGR2 aptamer sequence was obtained from Wu et al.,[48] containing a 17 base-long spacer sequence at the 5′-terminus (the original primer sequence used in the aptamer selection process[48]), followed by the 33 base-long binding region as follows: 5′-TCT-CGG-ACG-CGT-GTG-GTC-GGG-TGG-GAG-TTG-TGG-GGG-GGG-GTG-GGA-GGG-TT-3′. The aptamers were purchased with either a 5′-amino modification or a 5′-amino modification and 3′-Cy5 fluorescent dye modification from Integrated DNA Technologies. The AGR2 protein was purchased from MyBioSource Inc. Pancreatin from a porcine pancreas (4× USP), N_α-benzoyl-L-arginine ethyl ester (BAEE), trypsin, and BSA were purchased from Merck. Rabbit immunoglobulin G (IgG) was purchased from Jackson ImmunoResearch Laboratories Inc. Phosphate buffered saline (PBS, 10 mM) was composed of 137 mM NaCl, 2.7 mM KCl, 10 mM Na$_2$HPO$_4$, and 2 mM KH$_2$PO$_4$ (pH 7.0). The selection buffer (SB) was composed of 137 mM NaCl, 20 mM KCl, 10 mM Na$_2$HPO$_4$, and 2 mM KH$_2$PO$_4$ (pH 7.4). The 0.5 M MES buffer was prepared from 0.27 M MES and 0.23 M MES sodium salt (pH 6.1), and the Tris buffer was composed of 50 mM Tris base (pH 7.4).

2.2. Aptasensor Construction

2.2.1. Fabrication of Oxidized PSi Nanostructures. PSi Fabry−Pérot thin films were fabricated from a highly doped p-type crystalline Si wafers with typical resistivities of 0.90−0.95 mΩ·cm using a two-step anodization process. A detailed description of the etching setup can be found elsewhere.[49] First, a sacrificial layer was etched at a constant current density of 300 mA cm^{-2} for 30 s in a 3:1 (v/v) solution of aqueous HF (48%) and ethanol, respectively. Subsequently, the obtained porous layer was dissolved in 0.1 M NaOH and removed. Finally, a second etching was conducted under similar conditions, and the resultant freshly etched PSi was thermally oxidized in a tube furnace (Thermo Scientific, Lindberg/Blue M 1200 °C Split-Hinge) at 800 °C for 1 h in ambient air.[30]

2.2.2. Nanostructure Characterization with Scanning Electron Microscopy. The oxidized PSi nanostructure, pore diameter, and film thickness were characterized by high-resolution scanning electron microscopy (Carl Zeiss Ultra Plus) at an accelerating voltage of 1 keV.

2.2.3. Immobilization of Anti-AGR2 Aptamers. Amino-terminated aptamers were conjugated to the oxidized PSi films by amino silanization and carbodiimide coupling chemistry.[23,50] Initially, the oxidized PSi film was amino-silanized by incubation in a solution of 1% v/v APTES and 1% v/v DIEA in ddH$_2$O for 1 h, followed by washing with ddH$_2$O and ethanol and drying under a nitrogen stream. Subsequently, the PSi samples were annealed at 100 °C for 15 min. Next, carboxylation was achieved by incubation in a solution of succinic anhydride (10 mg mL^{-1}) and 2% v/v DIEA in ACN for 3 h, followed by extensive rinsing with ACN and ddH$_2$O and drying under a nitrogen stream. The samples were then reacted with EDC (10 mg mL^{-1}) and NHS (5 mg mL^{-1}) in MES buffer for 1 h, after which the samples were rinsed with MES buffer and gently dried under a nitrogen stream. Subsequently, an aptamer solution (50 μM in PBS) was applied, and the sample was incubated for 1 h, followed by rinsing

with Tris buffer to deactivate remaining reactive NHS and EDC groups on the surface. Finally, the aptamer-functionalized PSi was exposed to boiling ddH$_2$O for 2 min and then gently dried under a nitrogen stream to unfold any secondary structures of the aptamer prior to further use.

2.2.4. Chemistry Characterization with Fourier Transform Infrared (FTIR) Spectroscopy. The chemical modification of the PSi was studied with attenuated total reflectance FTIR (ATR-FTIR) spectroscopy, utilizing a Thermo 6700 FTIR instrument equipped with a Smart iTR diamond ATR device.

2.2.5. Chemistry Characterization with Confocal Laser Scanning Microscopy. The Cy5-labeled aptamer was immobilized onto the PSi, followed by scanning with a confocal laser scanning microscope (LSM 700, Carl Zeiss, Inc.) linked to a Zeiss inverted microscope that was equipped with a Zeiss X63 oil immersion objective. PSi photoluminescence (PL) and Cy5-labeled aptamers were excited with laser lines of 405 and 639 nm, respectively. For three-dimensional image projection of the porous structure, z-scans in 0.4 μm increments over a depth of ~12 μm were taken and projected with a standard Carl Zeiss software (ZEN 2009). Further image analysis was performed by Imaris Bitplane scientific software.

2.3. PDMS Microchannels

PDMS microchannels, 3 cm in length, 100−350 μm in width, and 20 μm in depth were fabricated in-house based on an SU8 template, which was constructed by standard lithography at Stanford Micro-fluidic Foundry (Stanford University, Stanford, CA, http://www.stanford.edu/group/foundry/).[51] PDMS polymer and cross-linker were mixed at a 10:1 ratio, respectively, followed by curing at 100 °C for 3 h. The microchannels were attached to the aptamer-functionalized PSi by exposing the inner surface of the PDMS to a corona treatment for 40 s using a laboratory corona treater (BD-20 V Electro-Technic Products), followed by baking at 100 °C for 3 h.

2.4. Time-Resolved Mass Transfer Visualization

The infiltration of a fluorescent-labeled AGR2 protein (Atto-647N dye) into the aptasensor was monitored in real time by confocal laser scanning microscopy (CLSM). Scans were conducted with a LSM 510 confocal laser-scanning microscope (Carl Zeiss, Inc.) linked to a Zeiss upright microscope that was equipped with a Zeiss X63 oil immersion objective. PSi PL and Atto-647N-labeled AGR2 were excited with laser lines of 458 and 633 nm, respectively. For three-dimensional image projection of the porous structure, z-scans in 0.73 μm increments over a depth of ~15 μm were taken every 30 s and projected with a standard Carl Zeiss software (ZEN 2010). Initially, the PL and AGR2 fluorescence signals were scanned within the aptasensor with 10 μL of SB buffer for 10 min. Then, a 1 μM solution of Atto-647N-labeled AGR2 in SB (40 μL) was introduced, and the PL and AGR2 fluorescence were measured continuously for additional 50 min. We used a relatively low AGR2 concentration for the measurements to obtain a time-resolved visualization of the protein infiltration before signal saturation was reached. Image analysis was performed by Imaris Bitplane scientific software.

2.5. Isotachophoresis (ITP) Assay

For the application of ITP, the freshly etched PSi was thermally oxidized in a tube furnace (Thermolyne) at 1000 °C for 46 h under a constant oxygen flow of 0.5 L min^{-1}. These harsh oxidation conditions are employed to ensure an insulting oxide layer capable of withstanding high voltage values.[31,45] Following aptamer immobilization, PDMS microchannels were attached (350 μm in width and 20 μm in height) as described above. Fluorescent-labeled AGR2 was used to visualize the protein focusing, where the protein was labeled via amine groups with Atto-647N dye to maintain its natural charge. In a standard cationic ITP assay, the microchannel and its east reservoir were filled with a leading electrolyte (LE) buffer using a vacuum pump, while the microchannel's west reservoir was filled with the fluorescent-labeled AGR2 diluted in a terminating electrolyte (TE) buffer; see schematic illustration in Figure S-1 (Supporting Information). A constant voltage of 350 V was then applied across the microchannel utilizing a high-voltage power supply

(model PS375, Stanford Research Systems, Inc.). The fluorescence signal was monitored with a customized Zeiss upright microscope, which was equipped with a camera (Axio Cam MRc, Zeiss), at a constant exposure time of 100 ms. An X-Cite 120Q excitation light source (Excelitas Technologies) was used for illumination. The LE and TE buffer compositions are detailed in Table S1 (Supporting Information). For the indirect anionic ITP assay, the LE was composed of 200 mM Bis-Tris, 100 mM KCl, and 100 mM HCl, and the TE buffer was composed of 20 mM Bis-Tris, 10 mM tricine, and 0.2 mM KCl. The fluorescent-labeled AGR2 was reacted with the anti-AGR2 aptamer at a ratio of 1:10, respectively, in TE buffer for 1 h prior to the ITP assay.

2.6. Biosensing Experiments

The aptasensor was mounted in a custom-made Plexiglas cell, and a tungsten light source was focused onto the center of the sample with a spot size of approximately 1 mm^2. Interferometric reflectance spectra were collected with a charge-coupled device (CCD) spectrometer (Ocean Optics, USB 4000) fitted with an objective lens coupled to a bifurcated fiber-optic cable; see Figure S-2a (Supporting Information) for additional details. For experiments in microchannels, a customized Zeiss upright microscope equipped with a CCD spectrometer was utilized. The aptasensor was fixed to the microscope stage under the objective and illuminated with light from a halogen source (halogen100 illuminator, Zeiss), which was focused through an A-Plan objective (10× magnification, 0.25 NA, Zeiss). The size of the illumination spot was controlled by the microscope iris and adjusted to the microchannel width (the experimental setup is shown in Figure S-2b in the Supporting Information).

Illumination and reflectivity detection were performed perpendicular to the surface, and the reflectance spectra were recorded in real time at a wavelength range of 450−900 nm. The collected spectra were analyzed by reflective interferometric Fourier transformation spectroscopy (RIFTS),[23,52,53] where taking the fast Fourier transformation (FFT) of the raw spectra results in a peak that corresponds to the dominant frequency of the Fabry−Pérot interference fringes. The position of this peak along the x-axis equals the effective optical thickness (EOT) of the porous layer and is the product of the average refractive index and the thickness of the porous layer. Reflectance spectra were recorded every 15 s throughout the experiments, and the data are presented as a relative EOT, which is defined as

$$\frac{\Delta EOT_t}{EOT_0} = \frac{EOT_t - EOT_0}{EOT_0}$$

where EOT_0 is the averaged EOT signal obtained during baseline establishment.

In all biosensing experiments, a baseline was first acquired in SB. Then, the protein solution (in SB or in a simulated pancreatic juice) was introduced, and the sample was incubated for 1 h. The protein solution was removed, and the aptasensor was extensively washed with SB. Please note that the purchased AGR2 stock (1 mg mL^{-1}) was diluted in 20 mM Tris-HCl, 1 mM DTT, 1 mM EDTA, and 10% glycerol (pH 8.0) buffer. Thus, its dilution in SB contains residues of these components. Biosensing experiments with nontarget proteins were carried out with the same dilution procedure to eliminate variability due to the buffer composition. For experiments with simulated pancreatic juice, pancreatin was utilized. It was diluted according to its trypsin activity to provide 100 p-toluene-sulfonyl-L-arginine methyl ester units per milliliter.[54] The trypsin activity of 0.45 μm filtered pancreatin in SB was determined by a standard BAEE assay[55] and diluted accordingly. The total protein amount within this sample was determined with a NanoDrop instrument (NanoDrop 2000 spectrophotometer, Thermo Scientific), and the sample was analyzed by standard SDS-PAGE. In some experiments, mixing was applied by manually pipetting the AGR2 solution over the aptasensor for 10 min, followed by an incubation without mixing. As a control, the buffer used for the dilution of the AGR2 protein stock was mixed for the same time on top of the aptasensor.

The limit of detection (LOD) was calculated based on the standard deviation of the relative EOT signal, while the aptasensor was
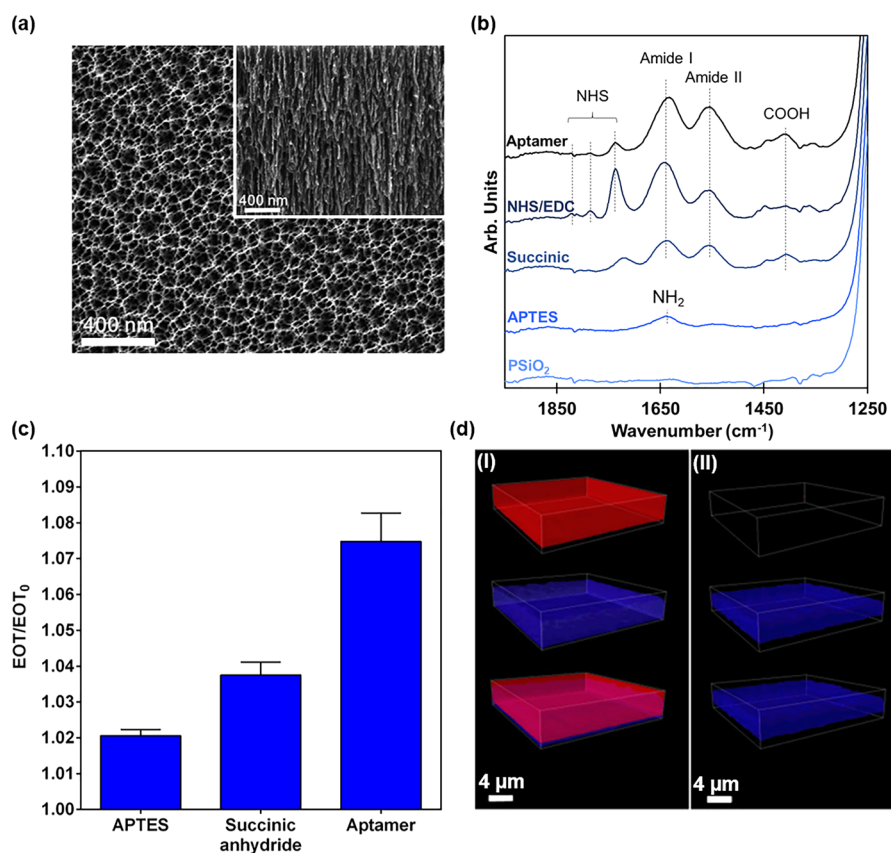
Figure 1. PSi aptasensor construction. (a) Top view and cross-section electron micrographs of the oxidized PSi film fabricated by anodization at 300 mA cm^{-2} for 30 s. (b) ATR-FTIR spectra and (c) relative EOT values of the PSi film following the synthetic steps for the aptamer immobilization: amino-silanization with APTES, carboxylation with succinic anhydride, activation with NHS/EDC, and the coupling of the amino-terminated aptamer. Note that the ATR-FTIR spectra are normalized to the Si–O–Si stretching peak, which is the maximal peak value for each spectrum, and that the EOT values are normalized to the EOT of a neat oxidized PSi film (no aptamer). Since NHS and EDC serve as leaving groups and were replaced by the aptamers, the EOT of the porous layer after NHS/EDC activation is not presented. (d) CLSM 3D projection images of the PSi film conjugated with a Cy5-labeled aptamer in the following cases: (I) full conjugation chemistry and (II) control experiment with no activation of the carboxylated surface with coupling agents NHS and EDC. The top row represents the fluorescence signal of the Cy5-labeled aptamer, the middle row represents the PL of the PSi nanostructure, and the bottom row is the merged view of the top and middle rows.

incubated with the baseline buffer prior to protein introduction. We use the lowest standard deviation values in each of the experimental setups, which are equal to $\sigma = 0.03$, $\sigma = 0.01$, and $\sigma = 0.04$ (as $\Delta EOT/EOT_0$ x10^{-3}) for the cell, mixing, and microchannel setups, respectively. The LOD is commonly determined as the concentration at which the signal equals $3.3*\sigma$, thus centering the noise floor around 0; however, this assumes that the intercept of the line of the best fit is 0, which is not always the case due to baseline drift or nonspecific adsorption. This may result in an undefined LOD when the intercept is outside the noise floor. Thus, we apply a more accurate and robust approach by centering the noise floor around the intercept and calculating the LOD as the concentration at which the signal exceeds its intercept by $3.3*\sigma$ in the linear fit of the data.[47] It should be noted that AGR2 is present in a dimer–monomer equilibrium;[56] thus, we utilized the molecular mass of the dimer to convert between micrograms per liter and molar units.

The apparent dissociation constant (K_D) was calculated based on a nonlinear regression of the obtained data utilizing the model for specific binding with a hill slope according to

$$Y = \frac{B_{max} \cdot X^h}{(K_D{}^h \cdot X^h)} \tag{2}$$

B_{max} is the concentration at which the maximum biosensor response is reached, and h is the Hill coefficient that gives information about the stoichiometry of the binding interaction.[57,58] GraphPad Prism software was used for the fitting.

2.7. Signal Processing Based on Morlet Wavelet Filtering and the Average Phase Difference (Morlet Wavelet Phase Method)

The acquired reflectance spectra were processed using the recently introduced Morlet wavelet phase method.[47] The requisite steps are depicted in Figure S-3 and include the application of complex Morlet wavelet band-pass filtering to the reflectance versus wavenumber spectrum. The Morlet wavelet parameters were determined based on the width and center frequency of the dominant peak in the FFT, which were obtained using a rectangular window. The phase of the resulting complex filtered spectrum was extracted and unwrapped. In this manner, the unwrapped phase was calculated for a reference spectrum during aptasensor incubation with the baseline buffer prior to protein or complex sample introduction and for each subsequent time point. The resulting Morlet wavelet phase signal is the average of the difference between the unwrapped phase of the reference spectrum and that of the spectrum collected at each time point.

2.8. Statistical Analysis

For all experimental sets, $n \geq 3$, and values are presented as the mean and the standard deviation of the mean. For statistical analysis, a Student's t-test was performed with a minimum confidence level of 0.05 for statistical significance, assuming unequal sample sizes and unequal variance.
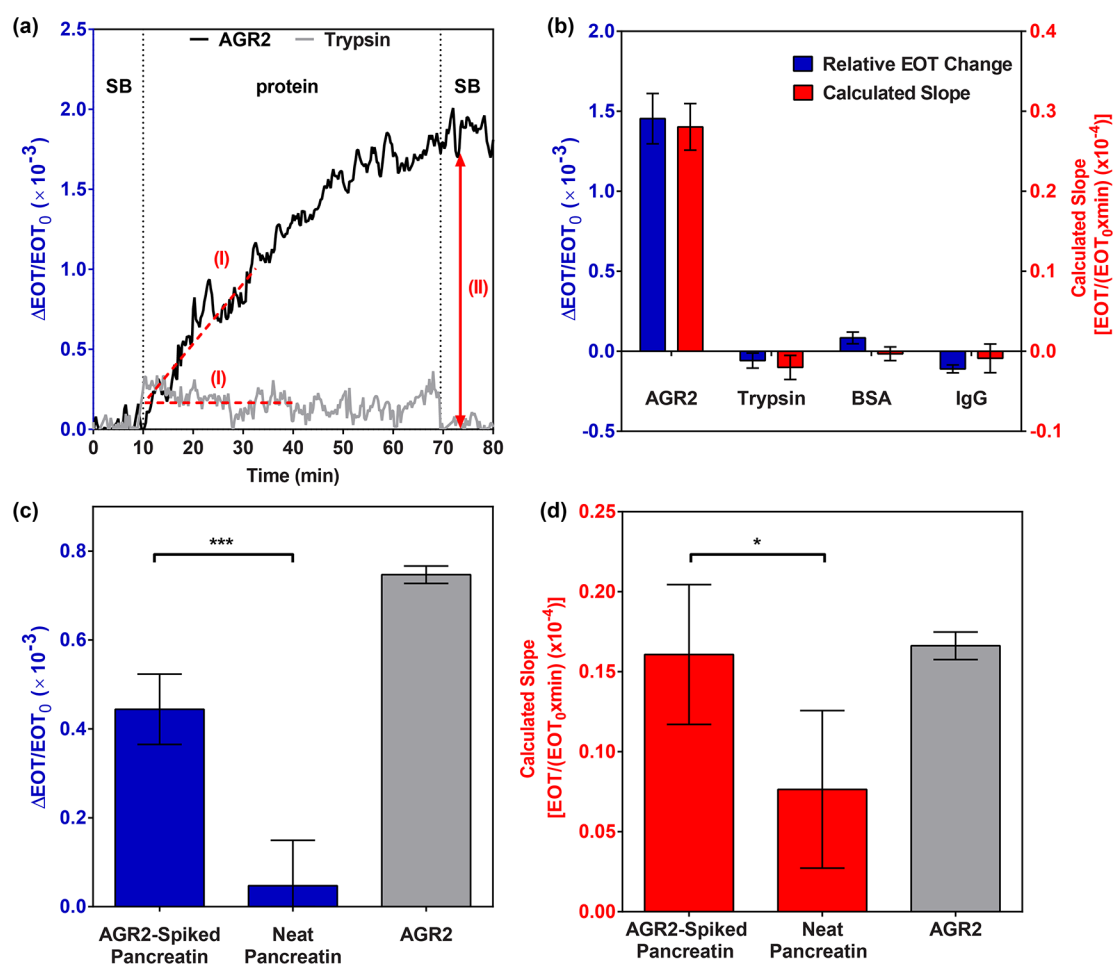
Figure 2. Aptasensor response to AGR2 in solution and in pancreatin. (a) Real-time relative EOT changes upon aptasensor incubation with AGR2 or trypsin protein solutions (200 μg mL^{-1}). The baseline was acquired in the aptamer's selection buffer (SB), followed by the introduction of the protein solution and incubation for 1 h. The slope of the real-time EOT curves at the initial 30 min of protein incubation (I) was used to study the protein infiltration rate into the porous layer and binding. The solution was removed, the biosensor was washed with SB, and the attained signal (II) is referred as the net relative EOT change. (b) Net relative EOT changes and calculated slopes upon exposure of the aptasensor to AGR2 and different nontarget proteins solutions (trypsin, BSA, and IgG; a similar concentration of 200 μg mL^{-1} was used in all experiments, $n = 3$). (c) Net relative EOT changes and (d) calculated slopes for pancreatin spiked with 100 μg mL^{-1} AGR2, neat pancreatin, and 100 μg mL^{-1} AGR2 in a buffer. ***/* Significantly different (t-test, $n = 3$ for neat AGR2 and $n = 5$ for experiments with pancreatin; $p = 0.0002$ for relative EOT changes and $p = 0.02$ for calculated slopes).

3. RESULTS AND DISCUSSION

3.1. Aptasensor Construction

PSi was fabricated by a contact-current anodization of Si to yield a nanostructured porous film (4.89 ± 0.07 μm thick) with characteristic interconnected cylindrical pores (with diameters of 40−60 nm), as presented in Figure 1a. The porous film was thermally oxidized and functionalized with amine-terminated anti-AGR2 aptamers[48] using NHS/EDC coupling chemistry,[50] where the aptamer is comprised of a 33 base-long binding region with a 17 base-long spacer sequence at its 5′-terminus[48] to increase the distance of the binding region from the solid surface.[59,60] The oxidized PSi was amino silanized, and the ATR-FTIR spectrum depicts a peak at 1640 cm^{-1} (see Figure 1b) that is attributed to the bending of the primary amines.[50,61] Subsequent carboxylation with succinic anhydride results in two strong peaks at 1557 and 1637 cm^{-1}, which are ascribed to amide II and amide I bonds, respectively, and a peak at 1406 cm^{-1} is assigned to the carboxylic acid groups.[50,61] After the activation with coupling agents EDC and NHS, three peaks at 1736, 1785, and 1820 cm^{-1} are visible,

which are characteristic of the NHS ester groups on the surface.[50,61,62] The latter diminish following the conjugation of the aptamer, while the peaks of the amide I and II bonds intensify. We also monitored the changes in the reflectance spectra of the PSi film throughout the aptamer immobilization process, and the relative EOT values after each modification step are presented in Figure 1c. Upon the immobilization of the different chemical groups and aptamer molecules, the average refractive index of the porous layer increases, as evidenced by the increasing EOT values.[49,52] The aptamer conjugation was further characterized by confocal laser scanning microscopy (CLSM), and Figure 1d presents 3D projection images of the PSi film following conjugation with the Cy5-labeled aptamer. When utilizing the complete conjugation chemistry of the labeled aptamer, a strong fluorescence signal from the labeled aptamer was observed to be uniformly distributed throughout the entire porous nanostructure (Figure 1d-I). As a control, the activation step of the carboxylated surface with NHS and EDC was omitted, and no fluorescence from the Cy5-labeled aptamer was

detected, indicating that no conjugation of the aptamers to the carboxylated surface occurred (Figure 1d-II). Thus, these results confirm the successful immobilization of the aptamer within the PSi nanostructure.

3.2. Biosensor Selectivity

Figure 2a presents the real-time relative EOT changes of the PSi aptasensor upon the introduction of the target (AGR2) and nontarget (Trypsin) proteins. The two proteins present similar molecular weights and charges, while trypsin is highly abundant in the gastrointestinal body fluids.[54] The aptasensor was initially washed with SB to allow the proper folding of the aptamer and to establish the initial EOT baseline. Following the introduction of AGR2, the EOT signal was observed to gradually increase due to the protein infiltration into the porous layer and binding to the tethered aptamers, as manifested by the slope of this curve. In contrast, for the nontarget trypsin only a low increase in the EOT signal was observed, remaining relatively steady throughout the incubation step. This was also observed for other relevant nontarget proteins, including BSA and IgG (see Figure S-4), and was also reported for other porous aptasensors.[23,63,64] While the slope of the real-time EOT signal cannot differentiate between infiltration and molecular binding phenomena,[65] the net increase in the relative EOT (obtained upon the wash step with SB intended for removal of unbound and adsorbed proteins) is used to study apparent protein binding within the PSi. Figure 2b summarizes both the averaged net EOT values and the slopes obtained in these experiments. Only minor changes were observed for the nontarget proteins, demonstrating the outstanding selectivity of the biosensor.

Pancreatic juice is a highly complex fluid rich with different proteins and digestive enzymes.[66] Given that pancreatic juice is secreted by the pancreas, it serves as an opportune medium for studying pancreatic cancer-related proteins and specifically early cancer-stage-related proteins, such as AGR2.[67−69] Thus, the aptasensor was challenged with pancreatin, which is a simulated pancreatic juice from pigs. It is composed of a mixture of several digestive enzymes, such as amylase, trypsin, lipase, ribonuclease, and protease, that are produced by the exocrine cells of the porcine pancreas.[54] The total protein concentration is 19 ± 1 mg mL^{-1}, and the abundancy of nontarget proteins within this sample is shown in an SDS-PAGE analysis in Figure S-5 (Supporting Information). The aptasensor response in terms of the net EOT change to the neat and AGR2-spiked pancreatin is presented in Figure 2c. Pancreatin induced only a small increase in the net relative EOT, which is suggestive of nonspecific binding, while the spiked samples result in ninefold higher EOT changes (t-test, $p = 0.0002$). This further highlights the selectivity of the aptasensor, where AGR2 is selectively bound while outnumbered >100-fold by nontarget proteins. Yet, it should be noted that the response to the spiked pancreatin was lower than that obtained for AGR2 in the buffer (Figure 2c). This result may be ascribed to pancreatin components interfering with the aptamer-AGR2 binding, which is highly dependent on the proper folding of the aptamer.[70]

The calculated slopes (see Figure 2d) also present the selectivity of the biosensor toward AGR2, as the AGR2-spiked pancreatin induced a twofold higher slope compared to that of neat pancreatin (t-test, $p = 0.02$). Yet, the attained slope signal in neat pancreatin is rather high, and the coefficient of variation between readouts is prominent compared to the net relative

EOT change (Figure 2c). The different behaviors of these two signal analysis approaches stem from their origin; while the slope characterizes the protein infiltration and apparent binding rate, the net relative EOT signal represents the total binding within the porous layer. Thus, in contrast to the biosensor performance in a single protein solution (Figure 2b), some of the components of this concentrated complex protein mixture diffuse into the porous nanostructure and nonspecifically adsorb on the pore walls upon overwhelming the aptasensor with pancreatin, resulting in a higher slope as shown in Figure 2d. This can be observed in Figure S-6 (Supporting Information), which presents the real-time increase in the relative EOT during neat pancreatin introduction. Yet after ∼25 min of incubation the signal reaches a plateau, whereas for the spiked sample the signal continues to increase throughout the incubation period, resembling the real-time response of the aptasensor to AGR2 in a buffer. Once the aptasensor is washed with SB, the EOT decreases by 6 ± 1 and 5.6 ± 0.3 nm for the neat and spiked pancreatin, respectively (corresponding to relative EOT decrease of 0.5 ± 0.1 and 0.40 ± 0.02 $\Delta EOT/EOT_0 \times 10^{-3}$, respectively), indicating a similar extent of removal of adsorbed and nonspecifically bound proteins from the porous layer. As such, due to the wash step the net EOT change (presented in Figure 2c) is less affected by reversible adsorption and nonspecific binding.

3.3. Limit of Detection

Figure 3 presents the averaged net relative EOT changes and calculated slopes upon exposure of the biosensor to different
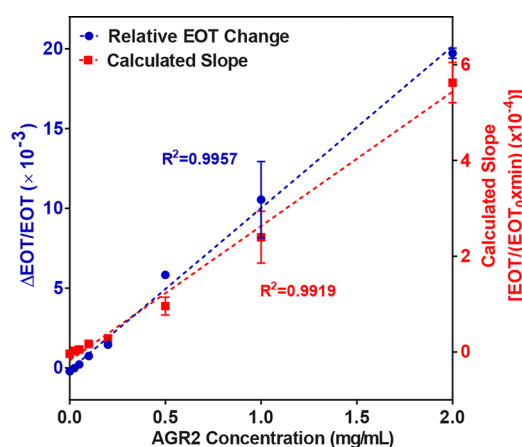

Figure 3. Net relative EOT changes and calculated slopes upon exposure of aptamer-functionalized PSi to different concentrations of AGR2, presenting a linear correlation to both signal parameters ($n = 3$).

concentrations of AGR2. The linear detection range of the biosensor is between 0.05 and 2 mg mL^{-1} based on both signal analysis methods, with a good linear correlation ($R^2 = 0.9957$ for the relative EOT changes and $R^2 = 0.9919$ for the calculated slope). For the net relative EOT signal, a concentration of 50 μg mL^{-1} is detected with an average signal-to-noise ratio (SNR) of 4.5, and the theoretical LOD value is calculated as 9.2 μg mL^{-1} (∼0.2 μM). Nevertheless, in practice an AGR2 concentration of 25 μg mL^{-1} did not result in a reliable signal and cannot be differentiated from the background noise. Furthermore, the apparent dissociation constant is 21 ± 1 μM, which is several orders of magnitude

higher than the reported value for that of the anti-AGR2 aptamer (determined to be in the nanomolar range by flow cytometry analysis in solution).[48] This is in accordance with our previous report where the protein diffusion was found to have a profound effect on its capture rate, resulting in micromolar apparent dissociation constants and detection limits regardless of the capture probe and the protein target pair.[65]

Herein, we experimentally demonstrate this phenomenon by real-time confocal laser scanning microscopy (CLSM) imaging of the diffusion process of a fluorescent-labeled AGR2 into an aptamer-functionalized PSi. We monitored the real-time fluorescence signal of the labeled protein with respect to the intrinsic photoluminescence (PL) signal of the PSi skeleton,[71,72] allowing us to spatially correlate the labeled protein molecules with respect to the porous nanostructure.[50,73,74] Figure 4a presents CLSM 3D projection images of the aptasensor, prior and 1 min after introduction of the fluorescent-labeled AGR2. The images were acquired by stacking 0.73 μm CLSM cross sections and present both the porous layer region, as well as the solution above the pores. These demonstrate that 1 min after the introduction of AGR2, the protein fluorescence signal is observed mainly above the porous layer, with a lower intensity signal within the porous layer. Figure 4b presents the distribution of the AGR2 fluorescence signal and the PSi PL signal with depth, in a segment of 10.95 μm. The location of the porous layer, which is 4.89 $\pm$ 0.07 μm thick (according to SEM measurements), is estimated based on the PL peak maximum, attributed to the top region of the PSi. Thus, the region of <3 μm represents the solution phase, above the pore entry. The fluorescence intensity of the protein increases with time in the imaged region and varies with depth within the PSi layer. A distinct gradient is observed at all studied time points, where the highest signal is measured at the bulk solution (above the pore entry) and the lowest at the bottom of the porous layer. These results qualitatively illustrate the target's concentration gradient and indicate that equilibration was not reached within 40 min. This is in agreement with the results of the biosensing experiments, where the EOT signal does not reach saturation in this time frame, see Figure 2a. Thus, we can conclude that molecular diffusion processes affect protein delivery to the porous layer, for at least 40 min after initial protein introduction to the biosensor, and that mass transport acceleration is mandatory for improving the biosensor response time and accordingly its sensitivity in this time frame.
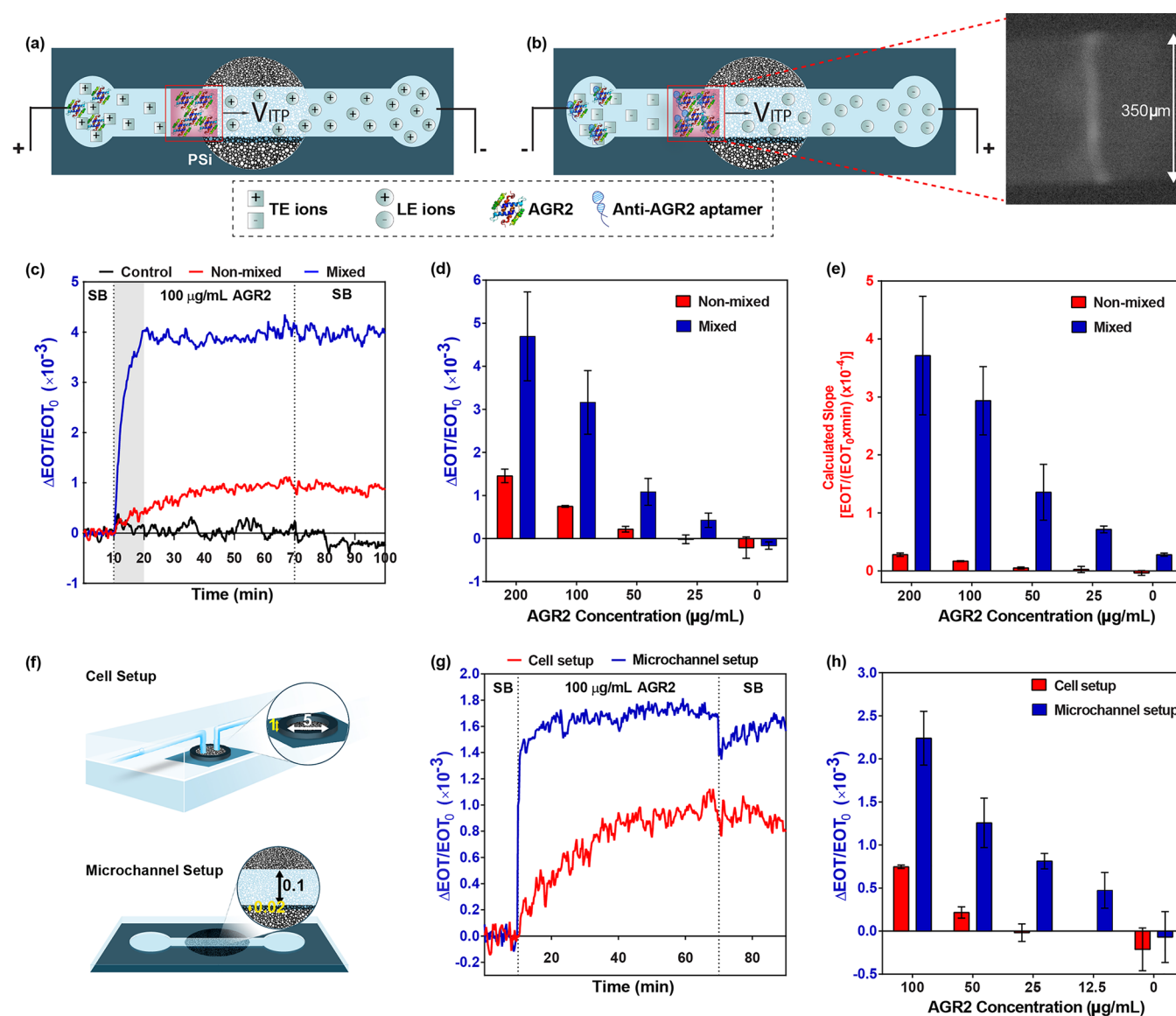
3.4. Mass Transfer Acceleration

The target flux to the biosensor surface is governed by Fick's laws of diffusion and is both correlated to the target concentration gradient and inversely proportional to the diffusion path length. Thus, increasing the target concentration gradient and decreasing the diffusion path length will result in enhanced diffusion flux. In our previous work,[45] we incorporated the isotachophoresis (ITP) technique for the on-chip and real-time concentration of a target protein in the sample, thus locally increasing the target concentration gradient on top of the aptasensor and consequently improving its flux. This resulted in up to 1000-fold improvement in the LOD to the lower nanomolar range (measured values). In ITP, a discontinuous buffer system is used, which is comprised of a leading electrolyte (LE) and a terminating electrolyte (TE) that has higher and lower electrophoretic mobility than the
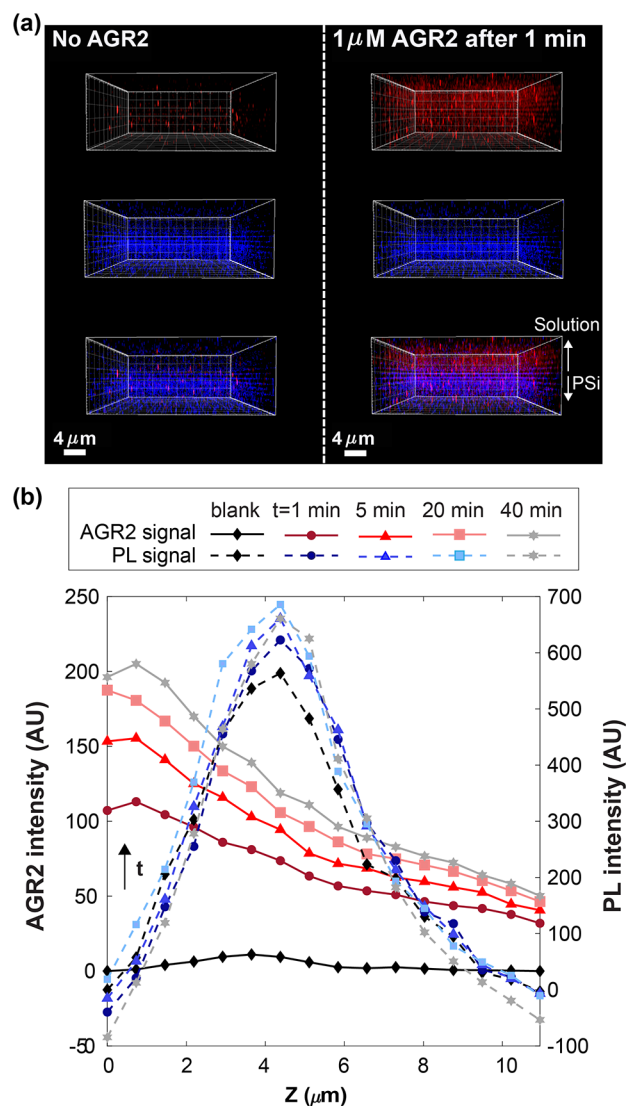
Figure 4. Time-resolved confocal laser scanning microscopy (CLSM) imaging of AGR2 diffusion within the aptasensor. (a) 3D projection images of the aptasensor before and 1 min after the introduction of fluorescent-labeled AGR2 (1 μM). 3D images were obtained from the stacking of CLSM cross sections. The top row represents the fluorescence signal of the fluorescent protein, the middle row represents the PL signal of the PSi nanostructure, and the bottom row is the merged view of the top and middle rows. (b) Variation with time of both the AGR2 fluorescence and the PL intensity as a function of depth (Z) above and within the porous nanostructure. The PSi region is estimated at the peak maximum of the PL signal, while the solution phase is located in the region of <3 μm. The gradient in the AGR2 intensity signal demonstrates that equilibration was not reached within the studied time frame.

target, respectively. Upon voltage application, a sharp electric field gradient is formed at the LE−TE interface, and any species having an intermediate electrophoretic mobility will focus at this interface. This results in the concentration of the target into a highly focused peak at the LE−TE interface.[75] The proper choice of the LE and TE buffer system is crucial for the success of the method and is highly dependent on the target characteristics, mainly its charge,[76] and the capture probe properties to ensure its functionality. While in our previous work anionic ITP was applied to concentrate a negatively charged protein,[45] in the present work, a cationic

Figure 5. Strategies for enhancing the sensitivity by mass transfer acceleration via ITP, target mixing, and integration with microchannels. (a) Schematic illustration of a cationic ITP assay for AGR2 on-chip concentration. (b) Schematic illustration and raw fluorescence image of AGR2 (50 nM) and the anti-AGR2 aptamer complex focusing under anionic ITP conditions. (c) Characteristic relative EOT changes as a function of time for 10 min mixed and nonmixed AGR2 (100 $\mu g\ mL^{-1}$) biosensing experiments. As a control, selection buffer (SB) was mixed on the aptasensor for 10 min. The gray area indicates the mixing phase. (d) Averaged net relative EOT changes and (e) calculated slopes for the detection of different concentrations of AGR2 in mixed and nonmixed biosesing experiments ($n = 3$). (f) Schematic illustration of the PSi aptasensor integrated in the conventional cell setup and the PDMS microchannel setup. Dimensions are in millimeter units. (g) Characteristic real-time relative EOT changes upon aptasensor incubation with 100 $\mu g\ mL^{-1}$ AGR2 in SB either in a cell setup or in a microchannel setup. (h) Averaged net relative EOT changes for the detection of different concentrations of AGR2 in both experimental setups ($n = 3$).

ITP is applied as AGR2 is theoretically characterized by a basic isoelectric point (based on its amino-acid sequence). As most proteins are negatively charged at physiological conditions,[77] cationic ITP assays exist[77−83] but are less prevalent.

Figure 5a presents the concept of the ITP assay for focusing AGR2. The PSi aptasensor was incorporated in PDMS microchannels, which were 350 μm in width and 20 μm in height. A fluorescent AGR2 (labeled via amine groups) was utilized to visualize the protein focusing within the microchannel. We have investigated several buffer compositions of cationic ITP for the focusing and accumulation of AGR2 at the LE−TE interface, see Table S-1 (Supporting Information). The microchannel was initially filled with LE buffer, while the labeled AGR2 was mixed with the TE buffer in the reservoir.

Voltage application resulted in the migration of the LE−TE interface toward the PSi aptasensor, as evidenced by the electric field and RIFTS measurements (data not shown). Yet, none of the studied conditions led to a formation of a fluorescent protein peak. Thus, in an effort to improve the AGR2 electrophoretic behavior, we have allowed the negatively charged anti-AGR2 aptamer to interact with the protein (prior to voltage application), resulting in a complex with a predicted total negative charge. Indeed, when utilizing the established anionic ITP buffer composition,[45,76] a fluorescent peak was visible at the buffer interface (see Figure 5b), suggesting the successful focusing of the protein. Nevertheless, the fluorescence intensity observed was weak and the peak formed was unstable for a relatively high AGR2 concentration (50
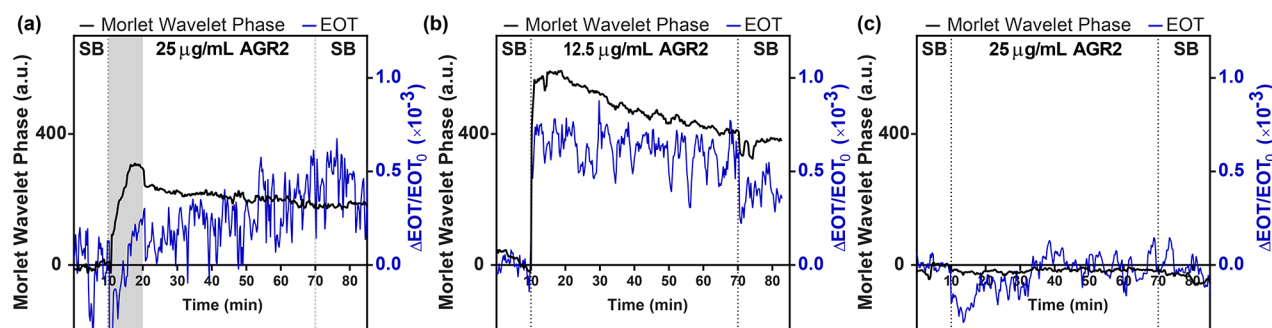
Figure 6. Characteristic changes in the relative Morlet wavelet phase and net EOT signals as a function of time for the lowest measured AGR2 concentrations in (a) mixing, (b) microchannel, and (c) cell setups, demonstrating that the Morlet wavelet phase signal processing technique reduces the signal noise and improves the SNR. The gray area indicates the mixing phase.

nM) compared to our previous work,[45] impeding the efficiency of the method. This emphasizes the main challenge of the ITP method, which should be carefully tailored for each target protein and capture probe pair.[84] We note that the further study and optimization of the buffer composition may eventually allow for the successful ITP-assisted concentration of AGR2.

Another strategy for enhancing the target flux to the biosensor is to reduce the diffusion length to the biosensor surface, which would result in a decrease in the diffusion time according to the following relation:

$$t \propto L^2/D$$

where L is the diffusion length and D is the target diffusion coefficient.[2,85,86] In the first approach, we mix the target solution on top of the biosensor, which eliminates the diffusion gradient in the bulk solution. Thus, a constant target concentration, equal to the applied solution concentration, can be assumed in the bulk solution, and the diffusion length is reduced to the porous layer thickness only. Figure 5c presents characteristic biosensing results for the aptasensor upon exposure to 100 μg mL^{-1} AGR2 and compares results between mixed and nonmixed systems. During mixing, a significantly higher apparent infiltration and binding rate (~6.5 fold) was obtained in comparison to the nonmixed system, and the relative EOT signal reached ~90% of the maximal signal obtained at equilibrium (after 1 h). Following the 10 min of mixing, the apparent binding rate sharply decreased, and minimal target capture was observed during the following incubation period. This is attributed to the decrease in the AGR2 concentration gradient, which is the driving force for diffusion, and suggests that the assay time can be reduced to 10 min of mixing with similar results. Figure 5d summarizes the averaged net relative EOT values upon exposure to different AGR2 concentrations for mixed and nonmixed systems. A signal enhancement greater than threefold was realized by target mixing for all studied AGR2 concentrations, and specifically an AGR2 concentration of 25 μg mL^{-1} was detected with an average SNR of 16. The calculated LOD was reduced by fivefold to 2.1 μg mL^{-1} (~47 nM). Analyzing the slope during the mixing allows us to study the apparent infiltration and binding kinetics, and a comparison to the nonmixed system is presented in Figure 5e. A substantial (>13-fold) enhancement for the mixed system was observed, underscoring the prominent effect of the enhanced target flux on the binding kinetics.

In the second approach, we decrease the characteristic diffusion length by integrating the PSi aptasensor with PDMS microchannels. Specifically, we decrease the solution height above the porous layer from 1 mm to 20 μm (as illustrated in Figure 5f). This in turn accelerated the target capture rate, where the EOT signal was observed to reach equilibration almost instantly, as shown in the real-time relative EOT curve in Figure 5g. Figure 5h compares the averaged net relative EOT changes for AGR2 detection in the cell and the microchannels, where for the latter a three- to sixfold increase in the EOT signal was observed compared to that for a cell setup. The calculated LOD in the microfluidic set up is 5.7 μg mL^{-1} (~129 nM) and, importantly, AGR2 can be reliably detected at a lower concentration of 12.5 μg mL^{-1} with an average SNR of 9 compared to a cell setup or mixing experiments. Note that due to the insufficient time resolution of the optical measurements at the initial protein introduction into the microchannel (see Figure S-7, Supporting Information), we do not analyze the binding slope of the real-time EOT curves.

The binding enhancement achieved by the two presented strategies emphasizes the limiting effect of diffusion in these porous biosensors. Further acceleration of the mass transfer rate can be achieved by the optimization of the porous nanostructure, e.g., by carefully adjusting the thickness of the porous layer (i.e., the use of thinner porous layers is beneficial as it reduces the diffusion length, but it also affects the reflectance and as a result may hamper the accuracy of the optical signal),[65] by introducing convection by the target flow in the system, and by optimizing the microchannel dimensions and geometry.[2,87] Additional improvement in the LOD can be achieved by stabilizing the aptasensor surface to reduce any negative signal drifting events, which are occasionally observed upon overtime measurements.

3.5. Improved Signal Processing

The aptasensor performance is also determined by the experimental setup, the signal processing technique, and consequently the noise of the system. To reduce the latter, we apply a different signal processing technique instead of RIFTS, named Morlet wavelet phase.[47] In this method, Morlet wavelet convolution is applied to the PSi reflectance spectra to filter out typical noise signatures. This results in enhanced noise immunity and consequently lower LOD values. In our recent study, we demonstrated that Morlet wavelet phase enables a one order of magnitude improvement in the LOD for BSA adsorption on a PSi thin film compared to RIFTS and other commonly used signal processing techniques.[35,46,47]

Figure 6 presents the real-time changes in the Morlet wavelet phase signal, compared to the RIFTS signal, for the lowest studied AGR2 concentrations in each of the different experimental setups, i.e., mixing, microchannel, and cell setups. Morlet wavelet phase analysis resulted in a significant reduction in the signal noise, which consequently improved the SNR between three to sixfold, compared to that of RIFTS (Figure 6a and 6b). Accordingly, the calculated LOD was improved for the mixing and microchannel experiments to 0.66 (~15 nM) and 0.97 μg mL^{-1} (~22 nM), respectively, where further improvement could be realized by optimizing the Morlet wavelet parameters to filter measured reflectance spectra more effectively. Importantly, the selectivity of the biosensor was maintained while utilizing Morlet wavelet phase analysis, see Figure S-8. Yet, as the platform is limited by the mass transfer rate, Morlet wavelet phase does not enable the detection of AGR2 at a concentration of 25 μg mL^{-1} in a cell setup (Figure 6c), where no signal was obtained with RIFTS as well. Thus, the lowest measured target concentration is unchanged upon Morlet wavelet phase analysis and mass transfer acceleration is mandatory for practical improvement in the biosensor sensitivity, where Morlet wavelet phase presents a complementary approach to improve the detection reliability.

4. CONCLUSIONS

We constructed a label-free PSi-based biosensor for detection of AGR2, a cancer biomarker, and studied different approaches for enhancing its sensitivity. The Anti-AGR2 aptamer was used as a capture probe and was immobilized within the nanoscale pores of the PSi thin film, which was utilized as an optical transducer. The detection of AGR2 by the aptamer-functionalized PSi film was carried out by the real-time monitoring of the reflectance changes of the PSi nanostructure. AGR2 capture by the aptasensor was confirmed by the net EOT signal increase, and the apparent infiltration and binding rate was calculated based on the analysis of the slope of the real-time EOT curves. Both signal analysis methods linearly correlate to the AGR2 concentration and enable the selective AGR2 detection both in a buffer and in a simulated pancreatic juice, where AGR2 is outnumbered >100-fold by nontarget proteins. The LOD of the aptasensor is limited to 9.2 μg mL^{-1} (0.2 μM), which is attributed to the slow diffusion rate to and within the porous layer. Thus, we applied several strategies to improve the target flux to the PSi aptasensor. The ITP technique, which allows the preconcentration of the target based on its electrophoretic mobility, was investigated for real-time focusing of the protein on top of the aptasensor. However, focusing of the positively charged AGR2 while maintaining the immobilized aptamer functionality was not successful. Two approaches were studied to reduce the diffusion length to the aptasensor, including target solution mixing on top of the biosensor and aptasensor integration in microchannels. Both methods successfully reduced the LOD of the aptasensor by up to fivefold and improved its response time from 1 h to several minutes. To further improve the detection reliability, the Morlet wavelet phase signal processing technique was applied instead of RIFTS and resulted in a substantial reduction in the measurement noise, which reduced the LOD to 0.66 μg mL^{-1} (15 nM). We acknowledge that the current LOD is not sufficient for AGR2 detection in real clinical samples and is inferior compared to other reported biosensors for AGR2 detection.[20−22] However, our constructed biosensor presents a superior simplicity and selectivity

in a highly complex media, as well as direct AGR2 detection with a real-time binding resolution. We also argue that the LOD can be improved by the additional means of nanostructure optimization in terms of its thickness,[65] introducing flow into the system for convection, the optimization of the microfluidic architecture,[87] applying active or passive mixing approaches (e.g., microfluidic mixers or magnetic mixers),[88,89] and tuning the filtering parameters of the Morlet wavelet phase method. Furthermore, surface stabilization and passivation can be applied by various blocking agents to improve the performance in the complex media and reduce signal drifts, and the signal can be further amplified by methods such as the utilization of a secondary capture probe, as we previously demonstrated.[24]

■ ASSOCIATED CONTENT

Ⓢ Supporting Information

The Supporting Information is available free of charge at https://pubs.acs.org/doi/10.1021/acsmeasuresciau.1c00019.

Details of the buffer compositions in the ITP assay, images of the experimental setups, Morlet wavelet phase signal processing steps, nontarget protein binding by the aptasensor or oxidized PSi, SDS-PAGE analysis of pancreatin, and real-time relative EOT changes of biosensing experiments with AGR2-spiked pancreatin or in a microfluidic device (PDF)

■ AUTHOR INFORMATION

Corresponding Author

Ester Segal − *Department of Biotechnology and Food Engineering and The Russell Berrie Nanotechnology Institute, Technion—Israel Institute of Technology, Haifa 3200003, Israel;* ⓞ orcid.org/0000-0001-9472-754X; Email: esegal@technion.ac.il

Authors

Sofia Arshavsky-Graham − *Department of Biotechnology and Food Engineering, Technion—Israel Institute of Technology, Haifa 3200003, Israel; Institute of Technical Chemistry, Leibniz Universität Hannover, 30167 Hanover, Germany*

Simon J. Ward − *Department of Electrical Engineering and Computer Science, Vanderbilt University, Nashville, Tennessee 37235, United States;* ⓞ orcid.org/0000-0003-0915-7584

Naama Massad-Ivanir − *Department of Biotechnology and Food Engineering, Technion—Israel Institute of Technology, Haifa 3200003, Israel*

Thomas Scheper − *Institute of Technical Chemistry, Leibniz Universität Hannover, 30167 Hanover, Germany*

Sharon M. Weiss − *Department of Electrical Engineering and Computer Science, Vanderbilt University, Nashville, Tennessee 37235, United States;* ⓞ orcid.org/0000-0003-2252-3104

Complete contact information is available at:
https://pubs.acs.org/10.1021/acsmeasuresciau.1c00019

Notes

The authors declare no competing financial interest.

■ REFERENCES

(1) Kelley, S. O. What Are Clinically Relevant Levels of Cellular and Biomolecular Analytes? *ACS Sensors* **2017**, *2* (2), 193−197.

(2) Wu, Y.; Tilley, R. D.; Gooding, J. J. Challenges and Solutions in Developing Ultrasensitive Biosensors. *J. Am. Chem. Soc.* **2019**, *141* (3), 1162−1170.

(3) Kelley, S. O.; Mirkin, C. A.; Walt, D. R.; Ismagilov, R. F.; Toner, M.; Sargent, E. H. Advancing the speed, sensitivity and accuracy of biomolecular detection using multi-length-scale engineering. *Nat. Nanotechnol.* **2014**, *9* (12), 969−980.

(4) Gooding, J. J.; Gaus, K. Single-Molecule Sensors: Challenges and Opportunities for Quantitative Analysis. *Angew. Chem., Int. Ed.* **2016**, *55* (38), 11354−11366.

(5) Giljohann, D. A.; Mirkin, C. A. Drivers of biodiagnostic development. *Nature* **2009**, *462* (7272), 461−464.

(6) Downs, A. M.; Gerson, J.; Hossain, M. N.; Ploense, K.; Pham, M.; Kraatz, H. B.; Kippin, T.; Plaxco, K. W. Nanoporous Gold for the Miniaturization of In Vivo Electrochemical Aptamer-Based Sensors. *ACS Sens* **2021**, *6* (6), 2299−2306.

(7) Borrebaeck, C. A. K. Precision diagnostics: moving towards protein biomarker signatures of clinical utility in cancer. *Nat. Rev. Cancer* **2017**, *17* (3), 199−204.

(8) Henry, N. L.; Hayes, D. F. Cancer biomarkers. *Mol. Oncol.* **2012**, *6* (2), 140−146.

(9) Edgell, T. A.; Barraclough, D. L.; Rajic, A.; Dhulia, J.; Lewis, K. J.; Armes, J. E.; Barraclough, R.; Rudland, P. S.; Rice, G. E.; Autelitano, D. J. Increased plasma concentrations of anterior gradient 2 protein are positively associated with ovarian cancer. *Clin. Sci.* **2010**, *118* (12), 717−725.

(10) Tian, S.-B.; Tao, K.-X.; Hu, J.; Liu, Z.-B.; Ding, X.-L.; Chu, Y.-N.; Cui, J.-Y.; Shuai, X.-M.; Gao, J.-B.; Cai, K.-L.; Wang, J.-L.; Wang, G.-B.; Wang, L.; Wang, Z. The prognostic value of AGR2 expression in solid tumours: a systematic review and meta-analysis. *Sci. Rep.* **2017**, *7* (1), 15500.

(11) Luu, T.-T.-T.; Bach, D.-H.; Kim, D.; Hu, R.; Park, H. J.; Lee, S. K. Overexpression of AGR2 Is Associated With Drug Resistance in Mutant Non-small Cell Lung Cancers. *Anticancer Res.* **2020**, *40* (4), 1855−1866.

(12) Ondrouskova, E.; Sommerova, L.; Nenutil, R.; Coufal, O.; Bouchal, P.; Vojtesek, B.; Hrstka, R. AGR2 associates with HER2 expression predicting poor outcome in subset of estrogen receptor negative breast cancer patients. *Exp. Mol. Pathol.* **2017**, *102* (2), 280−283.

(13) Rodríguez-Blanco, G.; Zeneyedpour, L.; Duijvesz, D.; Hoogland, A. M.; Verhoef, E. I.; Kweldam, C. F.; Burgers, P. C.; Smitt, P. S.; Bangma, C. H.; Jenster, G.; van Leenders, G. J. L. H.; Dekker, L. J. M.; Luider, T. M. Tissue proteomics outlines AGR2 AND LOX5 as markers for biochemical recurrence of prostate cancer. *Oncotarget* **2018**, *9* (92), 36444−36456.

(14) Tian, S.; Hu, J.; Tao, K.; Wang, J.; Chu, Y.; Li, J.; Liu, Z.; Ding, X.; Xu, L.; Li, Q.; Cai, M.; Gao, J.; Shuai, X.; Wang, G.; Wang, L.; Wang, Z. Secreted AGR2 promotes invasion of colorectal cancer cells via Wnt11-mediated non-canonical Wnt signaling. *Exp. Cell Res.* **2018**, *364* (2), 198−207.

(15) Dumartin, L.; Alrawashdeh, W.; Trabulo, S. M.; Radon, T. P.; Steiger, K.; Feakins, R. M.; di Magliano, M. P.; Heeschen, C.; Esposito, I.; Lemoine, N. R.; Crnogorac-Jurcevic, T. ER stress protein AGR2 precedes and is involved in the regulation of pancreatic cancer initiation. *Oncogene* **2017**, *36*, 3094.

(16) Chen, R.; Pan, S.; Duan, X.; Nelson, B. H.; Sahota, R. A.; de Rham, S.; Kozarek, R. A.; McIntosh, M.; Brentnall, T. A. Elevated level of anterior gradient-2 in pancreatic juice from patients with pre-malignant pancreatic neoplasia. *Mol. Cancer* **2010**, *9* (1), 149.

(17) Lennon, A. M.; Wolfgang, C. L.; Canto, M. I.; Klein, A. P.; Herman, J. M.; Goggins, M.; Fishman, E. K.; Kamel, I.; Weiss, M. J.; Diaz, L. A.; Papadopoulos, N.; Kinzler, K. W.; Vogelstein, B.; Hruban, R. H. The Early Detection of Pancreatic Cancer: What Will It Take to Diagnose and Treat Curable Pancreatic Neoplasia? *Cancer Res.* **2014**, *74* (13), 3381−3389.

(18) Wayner, E. A.; Quek, S.-I.; Ahmad, R.; Ho, M. E.; Loprieno, M. A.; Zhou, Y.; Ellis, W. J.; True, L. D.; Liu, A. Y. Development of an ELISA to detect the secreted prostate cancer biomarker AGR2 in voided urine. *Prostate* **2012**, *72* (9), 1023−1034.

(19) Shi, T.; Gao, Y.; Quek, S. I.; Fillmore, T. L.; Nicora, C. D.; Su, D.; Zhao, R.; Kagan, J.; Srivastava, S.; Rodland, K. D.; Liu, T.; Smith, R. D.; Chan, D. W.; Camp, D. G.; Liu, A. Y.; Qian, W.-J. A Highly Sensitive Targeted Mass Spectrometric Assay for Quantification of AGR2 Protein in Human Urine and Serum. *J. Proteome Res.* **2014**, *13* (2), 875−882.

(20) Hu, Y.; Li, L.; Guo, L. The sandwich-type aptasensor based on gold nanoparticles/DNA/magnetic beads for detection of cancer biomarker protein AGR2. *Sens. Actuators, B* **2015**, *209*, 846−852.

(21) Li, Z.; Miao, X.; Cheng, Z.; Wang, P. Hybridization chain reaction coupled with the fluorescence quenching of gold nano-particles for sensitive cancer protein detection. *Sens. Actuators, B* **2017**, *243*, 731−737.

(22) Białobrzeska, W.; Dziąbowska, K.; Lisowska, M.; Mohtar, M. A.; Muller, P.; Vojtesek, B.; Krejcir, R.; O'Neill, R.; Hupp, T. R.; Malinowska, N.; Bięga, E.; Bigus, D.; Cebula, Z.; Pala, K.; Czaczyk, E.; Żołędowska, S.; Nidzworski, D. An Ultrasensitive Biosensor for Detection of Femtogram Levels of the Cancer Antigen AGR2 Using Monoclonal Antibody Modified Screen-Printed Gold Electrodes. *Biosensors* **2021**, *11* (6), 184.

(23) Urmann, K.; Walter, J.-G.; Scheper, T.; Segal, E. Label-Free Optical Biosensors Based on Aptamer-Functionalized Porous Silicon Scaffolds. *Anal. Chem.* **2015**, *87* (3), 1999−2006.

(24) Urmann, K.; Reich, P.; Walter, J. G.; Beckmann, D.; Segal, E.; Scheper, T. Rapid and label-free detection of protein a by aptamer-tethered porous silicon nanostructures. *J. Biotechnol.* **2017**, *257*, 171−177.

(25) DeLouise, L. A.; Kou, P. M.; Miller, B. L. Cross-Correlation of Optical Microcavity Biosensor Response with Immobilized Enzyme Activity. Insights into Biosensor Sensitivity. *Anal. Chem.* **2005**, *77* (10), 3222−3230.

(26) Orosco, M. M.; Pacholski, C.; Miskelly, G. M.; Sailor, M. J. Protein-Coated Porous-Silicon Photonic Crystals for Amplified Optical Detection of Protease Activity. *Adv. Mater.* **2006**, *18* (11), 1393−1396.

(27) Ouyang, H.; DeLouise, L. A.; Miller, B. L.; Fauchet, P. M. Label-Free Quantitative Detection of Protein Using Macroporous Silicon Photonic Bandgap Biosensors. *Anal. Chem.* **2007**, *79* (4), 1502−1506.

(28) Moretta, R.; De Stefano, L.; Terracciano, M.; Rea, I. Porous Silicon Optical Devices: Recent Advances in Biosensing Applications. *Sensors* **2021**, *21* (4), 1336.

(29) Tieu, T.; Alba, M.; Elnathan, R.; Cifuentes-Rius, A.; Voelcker, N. H. Advances in Porous Silicon-Based Nanomaterials for Diagnostic and Therapeutic Applications. *Advanced Therapeutics* **2019**, *2* (1), 1800095.

(30) Kilian, K. A.; Bocking, T.; Gooding, J. J. The importance of surface chemistry in mesoporous materials: lessons from porous silicon biosensors. *Chem. Commun.* **2009**, No. 6, 630−640.

(31) Vilensky, R.; Bercovici, M.; Segal, E. Oxidized Porous Silicon Nanostructures Enabling Electrokinetic Transport for Enhanced DNA Detection. *Adv. Funct. Mater.* **2015**, 25 (43), 6725−6732.

(32) Zhao, Y.; Gaur, G.; Retterer, S. T.; Laibinis, P. E.; Weiss, S. M. Flow-Through Porous Silicon Membranes for Real-Time Label-Free Biosensing. *Anal. Chem.* **2016**, 88 (22), 10940−10948.

(33) Lazzara, T. D.; Mey, I.; Steinem, C.; Janshoff, A. Benefits and Limitations of Porous Substrates as Biosensors for Protein Adsorption. *Anal. Chem.* **2011**, 83 (14), 5624−5630.

(34) Rong, G.; Weiss, S. M. Biomolecule size-dependent sensitivity of porous silicon sensors. *Phys. Status Solidi A* **2009**, 206 (6), 1365−1368.

(35) Mariani, S.; Pino, L.; Strambini, L. M.; Tedeschi, L.; Barillaro, G. 10 000-Fold Improvement in Protein Detection Using Nano-structured Porous Silicon Interferometric Aptasensors. *ACS Sensors* **2016**, 1 (12), 1471−1479.

(36) Chhasatia, R.; Sweetman, M. J.; Prieto-Simon, B.; Voelcker, N. H. Performance optimization of porous silicon rugate filter biosensor for the detection of insulin. *Sens. Actuators, B* **2018**, 273, 1313−1322.

(37) Baranowska, M.; Slota, A. J.; Eravuchira, P. J.; Alba, M.; Formentin, P.; Pallarès, J.; Ferré-Borrull, J.; Marsal, L. F. Protein attachment to silane-functionalized porous silicon: A comparison of electrostatic and covalent attachment. *J. Colloid Interface Sci.* **2015**, 452, 180−189.

(38) Terracciano, M.; De Stefano, L.; Borbone, N.; Politi, J.; Oliviero, G.; Nici, F.; Casalino, M.; Piccialli, G.; Dardano, P.; Varra, M.; Rea, I. Solid phase synthesis of a thrombin binding aptamer on macroporous silica for label free optical quantification of thrombin. *RSC Adv.* **2016**, 6 (90), 86762−86769.

(39) Zhao, Y.; Gaur, G.; Mernaugh, R. L.; Laibinis, P. E.; Weiss, S. M. Comparative Kinetic Analysis of Closed-Ended and Open-Ended Porous Sensors. *Nanoscale Res. Lett.* **2016**, 11 (1), 395.

(40) De Stefano, L.; Orabona, E.; Lamberti, A.; Rea, I.; Rendina, I. Microfluidics assisted biosensors for label-free optical monitoring of molecular interactions. *Sens. Actuators, B* **2013**, 179, 157−162.

(41) Rea, I.; Orabona, E.; Lamberti, A.; Rendina, I.; De Stefano, L. A microfluidics assisted porous silicon array for optical label-free biochemical sensing. *Biomicrofluidics* **2011**, 5 (3), 034120.

(42) Mariani, S.; Paghi, A.; La Mattina, A. A.; Debrassi, A.; Dähne, L.; Barillaro, G. Decoration of Porous Silicon with Gold Nanoparticles via Layer-by-Layer Nanoassembly for Interferometric and Hybrid Photonic/Plasmonic (Bio)sensing. *ACS Appl. Mater. Interfaces* **2019**, 11 (46), 43731−43740.

(43) Balderas-Valadez, R. F.; Schurmann, R.; Pacholski, C. One Spot-Two Sensors: Porous Silicon Interferometers in Combination With Gold Nanostructures Showing Localized Surface Plasmon Resonance. *Front. Chem.* **2019**, 7, 593.

(44) Layouni, R.; Dubrovsky, M.; Bao, M.; Chung, H.; Du, K.; Boriskina, S. V.; Weiss, S. M.; Vermeulen, D. High contrast cleavage detection for enhancing porous silicon sensor sensitivity. *Opt. Express* **2021**, 29 (1), 1−11.

(45) Arshavsky-Graham, S.; Massad-Ivanir, N.; Paratore, F.; Scheper, T.; Bercovici, M.; Segal, E. On Chip Protein Pre-Concentration for Enhancing the Sensitivity of Porous Silicon Biosensors. *ACS Sensors* **2017**, 2 (12), 1767−1773.

(46) Mariani, S.; Strambini, L. M.; Barillaro, G. Femtomole Detection of Proteins Using a Label-Free Nanostructured Porous Silicon Interferometer for Perspective Ultrasensitive Biosensing. *Anal. Chem.* **2016**, 88 (17), 8502−8509.

(47) Ward, S. J.; Layouni, R.; Arshavsky-Graham, S.; Segal, E.; Weiss, S. M. Morlet Wavelet Filtering and Phase Analysis to Reduce the Limit of Detection for Thin Film Optical Biosensors. *ACS Sensors* **2021**, DOI: 10.1021/acssensors.1c00787.

(48) Wu, J.; Wang, C.; Li, X.; Song, Y.; Wang, W.; Li, C.; Hu, J.; Zhu, Z.; Li, J.; Zhang, W.; Lu, Z.; Yang, C. J. Identification, Characterization and Application of a G-Quadruplex Structured DNA Aptamer against Cancer Biomarker Protein Anterior Gradient Homolog 2. *PLoS One* **2012**, 7 (9), No. e46393.

(49) Sailor, M. J. *Porous Silicon in Practice: Preparation, Characterization and Applications*; John Wiley & Sons, 2012.

(50) Tenenbaum, E.; Ben-Dov, N.; Segal, E. Tethered Lipid Bilayers within Porous Si Nanostructures: A Platform for (Optical) Real-Time Monitoring of Membrane-Associated Processes. *Langmuir* **2015**, 31 (18), 5244−5251.

(51) Gerber, D.; Maerkl, S. J.; Quake, S. R. An in vitro microfluidic approach to generating protein-interaction networks. *Nat. Methods* **2009**, 6 (1), 71−74.

(52) Pacholski, C.; Sartor, M.; Sailor, M. J.; Cunin, F.; Miskelly, G. M. Biosensing Using Porous Silicon Double-Layer Interferometers: Reflective Interferometric Fourier Transform Spectroscopy. *J. Am. Chem. Soc.* **2005**, 127 (33), 11636−11645.

(53) Pacholski, C.; Yu, C.; Miskelly, G. M.; Godin, D.; Sailor, M. J. Reflective Interferometric Fourier Transform Spectroscopy: A Self-Compensating Label-Free Immunosensor Using Double-Layers of Porous SiO2. *J. Am. Chem. Soc.* **2006**, 128 (13), 4250−4252.

(54) Minekus, M.; Alminger, M.; Alvito, P.; Ballance, S.; Bohn, T.; Bourlieu, C.; Carriere, F.; Boutrou, R.; Corredig, M.; Dupont, D.; Dufour, C.; Egger, L.; Golding, M.; Karakaya, S.; Kirkhus, B.; Le Feunteun, S.; Lesmes, U.; Macierzanka, A.; Mackie, A.; Marze, S.; McClements, D. J.; Menard, O.; Recio, I.; Santos, C. N.; Singh, R. P.; Vegarud, G. E.; Wickham, M. S. J.; Weitschies, W.; Brodkorb, A. A standardised static in vitro digestion method suitable for food - an international consensus. *Food Funct.* **2014**, 5 (6), 1113−1124.

(55) Bergmeyer, H.*Methods of Enzymatic Analysis*, 2nd ed., Vol. 1; Academic Press: New York, NY, 1974; pp 515−516

(56) Patel, P.; Clarke, C.; Barraclough, D. L.; Jowitt, T. A.; Rudland, P. S.; Barraclough, R.; Lian, L.-Y. Metastasis-Promoting Anterior Gradient 2 Protein Has a Dimeric Thioredoxin Fold Structure and a Role in Cell Adhesion. *J. Mol. Biol.* **2013**, 425 (5), 929−943.

(57) Kurganov, B. I.; Lobanov, A. V.; Borisov, I. A.; Reshetilov, A. N. Criterion for Hill equation validity for description of biosensor calibration curves. *Anal. Chim. Acta* **2001**, 427 (1), 11−19.

(58) Hill, A. V. PROCEEDINGS OF THE PHYSIOLOGICAL SOCIETY: January 22, 1910. *J. Physiol.* **1910**, 40 (suppl), i−vii.

(59) Walter, J.-G.; Kökpinar, Ö.; Friehs, K.; Stahl, F.; Scheper, T. Systematic Investigation of Optimal Aptamer Immobilization for Protein-Microarray Applications. *Anal. Chem.* **2008**, 80 (19), 7372−7378.

(60) Urmann, K.; Modrejewski, J.; Scheper, T.; Walter, J.-G. Aptamer-modified nanomaterials: principles and applications. *BioNanoMaterials* **2017**, 18, 20160012.

(61) Kim, J.; Cho, J.; Seidler, P. M.; Kurland, N. E.; Yadavalli, V. K. Investigations of Chemical Modifications of Amino-Terminated Organic Films on Silicon Substrates and Controlled Protein Immobilization. *Langmuir* **2010**, 26 (4), 2599−2608.

(62) Voicu, R.; Boukherroub, R.; Bartzoka, V.; Ward, T.; Wojtyk, J. T. C.; Wayner, D. D. M. Formation, Characterization, and Chemistry of Undecanoic Acid-Terminated Silicon Surfaces: Patterning and Immobilization of DNA. *Langmuir* **2004**, 20 (26), 11713−11720.

(63) Arshavsky-Graham, S.; Urmann, K.; Salama, R.; Massad-Ivanir, N.; Walter, J.-G.; Scheper, T.; Segal, E. Aptamers vs. antibodies as capture probes in optical porous silicon biosensors. *Analyst* **2020**, 145 (14), 4991−5003.

(64) Pol, L.; Acosta, L. K.; Ferré-Borrull, J.; Marsal, L. F. Aptamer-Based Nanoporous Anodic Alumina Interferometric Biosensor for Real-Time Thrombin Detection. *Sensors* **2019**, 19 (20), 4543.

(65) Arshavsky Graham, S.; Boyko, E.; Salama, R.; Segal, E. Mass Transfer Limitations of Porous Silicon-Based Biosensors for Protein Detection. *ACS Sensors* **2020**, 5 (10), 3058−3069.

(66) Makawita, S.; Smith, C.; Batruch, I.; Zheng, Y.; Ruckert, F.; Grutzmann, R.; Pilarsky, C.; Gallinger, S.; Diamandis, E. P. Integrated proteomic profiling of cell line conditioned media and pancreatic juice for the identification of pancreatic cancer biomarkers. *Mol. Cell. Proteom.* **2011**, 10 (10), M111.008599.

(67) Makawita, S.; Smith, C.; Batruch, I.; Zheng, Y.; Rückert, F.; Grützmann, R.; Pilarsky, C.; Gallinger, S.; Diamandis, E. P. Integrated Proteomic Profiling of Cell Line Conditioned Media and Pancreatic Juice for the Identification of Pancreatic Cancer Biomarkers. *Mol. Cell. Proteom.* **2011**, *10* (10), No. M111.008599.

(68) Chen, R.; Pan, S.; Brentnall, T. A.; Aebersold, R. Proteomic Profiling of Pancreatic Cancer for Biomarker Discovery. *Molecular & Cellular Proteomics* **2005**, *4* (4), 523–533.

(69) Chen, R.; Pan, S.; Yi, E. C.; Donohoe, S.; Bronner, M. P.; Potter, J. D.; Goodlett, D. R.; Aebersold, R.; Brentnall, T. A. Quantitative proteomic profiling of pancreatic cancer juice. *Proteomics* **2006**, *6* (13), 3871–3879.

(70) Urmann, K.; Modrejewski, J.; Scheper, T.; Walter, J.-G. Aptamer-modified nanomaterials: principles and applications. *BioNano Materials* **2017**, *18*, 20160012.

(71) Canham, L. T. Silicon quantum wire array fabrication by electrochemical and chemical dissolution of wafers. *Appl. Phys. Lett.* **1990**, *57* (10), 1046–1048.

(72) Cullis, A. G.; Canham, L. T. Visible light emission due to quantum size effects in highly porous crystalline silicon. *Nature* **1991**, *353* (6342), 335–338.

(73) Shtenberg, G.; Massad-Ivanir, N.; Fruk, L.; Segal, E. Nanostructured Porous Si Optical Biosensors: Effect of Thermal Oxidation on Their Performance and Properties. *ACS Appl. Mater. Interfaces* **2014**, *6* (18), 16049–16055.

(74) Tenenbaum, E.; Segal, E. Optical biosensors for bacteria detection by a peptidomimetic antimicrobial compound. *Analyst* **2015**, *140* (22), 7726–7733.

(75) Everaerts, F. M.; Beckers, J. L.; Verheggen, T. P. E. M. *Isotachophoresis: Theory, Instrumentation and Applications*; Elsevier: New York, NY, 2011.

(76) Paratore, F.; Zeidman Kalman, T.; Rosenfeld, T.; Kaigala, G. V.; Bercovici, M. Isotachophoresis-Based Surface Immunoassay. *Anal. Chem.* **2017**, *89* (14), 7373–7381.

(77) Guo, S.; Jacroux, T.; Ivory, C. F.; Li, L.; Dong, W.-J. Immunobinding-induced alteration in the electrophoretic mobility of proteins: An approach to studying the preconcentration of an acidic protein under cationic isotachophoresis. *Electrophoresis* **2019**, *40* (9), 1314–1321.

(78) Jacroux, T.; Bottenus, D.; Rieck, B.; Ivory, C. F.; Dong, W.-J. Cationic isotachophoresis separation of the biomarker cardiac troponin I from a high-abundance contaminant, serum albumin. *Electrophoresis* **2014**, *35* (14), 2029–2038.

(79) Stutz, H.; Bordin, G.; Rodriguez, A. R. Capillary zone electrophoresis of metal-binding proteins in formic acid with UV- and mass spectrometric detection using cationic transient capillary isotachophoresis for preconcentration. *Electrophoresis* **2004**, *25* (7–8), 1071–1089.

(80) Kubačák, P.; Mikuš, P.; Valášiková, I.; Havránek, E. Simultaneous Determination of Essential Basic Amino Acids in Pharmaceuticals by Capillary Isotachophoresis. *Arch. Pharm.* **2006**, *339* (2), 96–99.

(81) Sázelová, P.; Kašička, V.; Šolínová, V.; Koval, D. Determination of purity degree and counter-ion content in lecirelin by capillary zone electrophoresis and capillary isotachophoresis. *J. Chromatogr. B: Anal. Technol. Biomed. Life Sci.* **2006**, *841* (1), 145–151.

(82) Bottenus, D.; Hossan, M. R.; Ouyang, Y.; Dong, W.-J.; Dutta, P.; Ivory, C. F. Preconcentration and detection of the phosphorylated forms of cardiac troponin I in a cascade microchip by cationic isotachophoresis. *Lab Chip* **2011**, *11* (22), 3793–3801.

(83) Qu, Y.; Marshall, L. A.; Santiago, J. G. Simultaneous Purification and Fractionation of Nucleic Acids and Proteins from Complex Samples Using Bidirectional Isotachophoresis. *Anal. Chem.* **2014**, *86* (15), 7264–7268.

(84) Eid, C.; Santiago, J. G. Isotachophoresis applied to biomolecular reactions. *Lab Chip* **2018**, *18* (1), 11–26.

(85) Zhu, W.; Wang, C.; Wang, H.; Li, G. Theory and simulation of diffusion-adsorption into a molecularly imprinted mesoporous film and its nanostructured counterparts. Experimental application for trace explosive detection. *RSC Adv.* **2014**, *4* (77), 40676–40685.

(86) Kant, K.; Yu, J.; Priest, C.; Shapter, J. G.; Losic, D. Impedance nanopore biosensor: influence of pore dimensions on biosensing performance. *Analyst* **2014**, *139* (5), 1134–1140.

(87) Lynn, N. S.; Sipova, H.; Adam, P.; Homola, J. Enhancement of affinity-based biosensors: effect of sensing chamber geometry on sensitivity. *Lab Chip* **2013**, *13* (7), 1413–1421.

(88) Lynn, N. S.; Bocková, M.; Adam, P.; Homola, J. Biosensor Enhancement Using Grooved Micromixers: Part II, Experimental Studies. *Anal. Chem.* **2015**, *87* (11), 5524–5530.

(89) Arshavsky-Graham, S.; Segal, E. Lab-on-a-Chip Devices for Point-of-Care Medical Diagnostics. *Adv. Biochem. Engin./Biotechnol.* **2020**, 1–19.